HHS Public Access

Author manuscript

J Neural Eng. Author manuscript; available in PMC 2022 September 15.

Published in final edited form as:

J Neural Eng. ; 18(5): . doi:10.1088/1741-2552/abf066.

Impact of brain shift on neural pathways in deep brain stimulation: a preliminary analysis via multi-physics finite element models

Ma Luo[1,2,*], **Saramati Narasimhan**[2,3], **Paul S Larson**[4], **Alastair J Martin**[5], **Peter E Konrad**[6], **Michael I Miga**[1,2,3]

[1]Department of Biomedical Engineering, Vanderbilt University, Nashville, TN, United States of America

[2]Vanderbilt Institute for Surgery and Engineering, Vanderbilt University, Nashville, TN, United States of America

[3]Department of Neurological Surgery, Vanderbilt University Medical Center, Nashville, TN, United States of America

[4]Department of Neurological Surgery, University of California, San Francisco, CA, United States of America

[5]Department of Radiology and Biomedical Imaging, University of California, San Francisco, CA, United States of America

[6]Department of Neurosurgery, West Virginia University, Morgantown, WV, United States of America

Abstract

Objective.—The effectiveness of deep brain stimulation (DBS) depends on electrode placement accuracy, which can be compromised by brain shift during surgery. While there have been efforts in assessing the impact of electrode misplacement due to brain shift using preop- and postop-imaging data, such analysis using preop- and intraop-imaging data via biophysical modeling has not been conducted. This work presents a preliminary study that applies a multi-physics analysis framework using finite element biomechanical and bioelectric models to examine the impact of realistic intraoperative shift on neural pathways determined by tractography.

Approach.—The study examined six patients who had undergone interventional magnetic resonance-guided DBS surgery. The modeling framework utilized a biomechanical approach to update preoperative MR to reflect shift-induced anatomical changes. Using this anatomically deformed image and its undeformed counterpart, bioelectric effects from shifting electrode leads could be simulated and neural activation differences were approximated. Specifically, for each configuration, volume of tissue activation was computed and subsequently used for tractography estimation. Total tract volume and overlapping volume with motor regions as well as connectivity

[*]Author to whom any correspondence should be addressed. m.luo@vanderbilt.edu.

profile were compared. In addition, volumetric overlap between different fiber bundles among configurations was computed and correlated to estimated shift.

Main results.—The study found deformation-induced differences in tract volume, motor region overlap, and connectivity behavior, suggesting the impact of shift. There is a strong correlation ($R = -0.83$) between shift from intended target and intended neural pathway recruitment, where at threshold of ~2.94 mm, intended recruitment completely degrades. The determined threshold is consistent with and provides quantitative support to prior observations and literature that deviations of 2–3 mm are detrimental.

Significance.—The findings support and advance prior studies and understanding to illustrate the need to account for shift in DBS and the potentiality of computational modeling for estimating influence of shift on neural activation.

Keywords

brain shift; computational modeling; deep brain stimulation; neurosurgery; tractography

1. Introduction

Deep brain stimulation (DBS) presents an adjustable and reversible surgical treatment option for symptom relief in patients with movement disorders. One particularly impactful application of DBS is the treatment of Parkinson's disease (PD), especially those with medically refractory tremor (Collins *et al* 2010). PD impacts 0.1%–0.2% of the population and 1% of the population over the age of 60 (Bratsos *et al* 2018). While there is a wealth of literature reports illustrating the effectiveness of DBS therapy, in a comprehensive recent review by Bratsos *et al*, eight randomized controlled trials were analyzed comparing outcome measures between DBS and best medical therapy (Bratsos *et al* 2018). Overall the study found in a total of 1189 patients (with sample sizes ranging 19–366 in eight different studies), DBS was determined to significantly improve the total Unified Parkinson's Disease Rating Scale, including all sub-scores (I–IV), as well as Parkinson's Disease Questionnaire while decrease levodopa equivalent dose (Bratsos *et al* 2018). While highly effective in providing better motor control and functionality for patients, the quality of DBS therapy may be compromised, i.e. dissatisfactory outcome or adverse events, by misplacement of DBS electrodes.

To probe the scope of the impact of suboptimal electrode placement on surgical outcome, Rolston *et al* performed an analysis to examine data on over 28 000 cases of DBS procedures from the Centers for Medicare and Medicaid Services (CMS) and the National Surgical Quality Improvement Program (NSQIP) databases, and reported that revision or removal occurred in 15.2% and 34.0% from CMS and NSQIP, respectively (Rolston *et al* 2016). The study speculated that ~48.5% of these revisions or removals was likely due to poor positioning of the electrode or inadequate clinical outcome and noted that this result is similar to previous analyses on failed DBS treatment where 46% of revisions were due to suboptimal placement of electrodes (Rolston *et al* 2016).

One contributing factor to the misplacement of electrodes is brain shift that ensues after burr hole and dural opening in DBS surgery. In a report by Luo *et al* (2020), a summary of various studies using preop- and postop-imaging data to gauge shift in DBS was provided, where shift at deep brain structures ranges from 1.5 to up to 4 mm. For example, Elias *et al* found anterior commissure shift above 2 mm in 7.6% of patients and above 1.5 mm in 13.6% ($n = 66$) (Elias *et al* 2007). When preop- and intraop-imaging data were used to assess brain shift, Ivan *et al* found deep brain structure shift above 2 mm in 9% of the study population and 1–2 mm in 20% ($n = 44$); additionally, cortical surface shift up to 10 mm was observed (Ivan *et al* 2014). From Elias *et al* and Ivan *et al*, it is apparent that brain shift during DBS burr hole surgery occurs in a considerable population of patients (Elias *et al* 2007, Ivan *et al* 2014). Addressing brain shift may reduce the incidents of revision or removal due to poorly positioned electrodes as stated in Rolston *et al* (2016), which would lead to better patient experience, reduce further potential surgical risk, enhance short- and long- term therapy outcome, and improve overall and longitudinal cost-effectiveness of DBS therapy. To date, the deviation threshold from an intended target has been based on clinical observations and speculations, and varies among studies as summarized in Luo *et al* (2020): e.g. 3 mm is mentioned in Balachandran *et al*, Anderson *et al* and McClelland *et al*; while 2 mm is suggested in Ivan *et al* and Kremer *et al* (McClelland *et al* 2005, Balachandran *et al* 2009, Ivan *et al* 2014, Anderson *et al* 2018, Kremer *et al* 2019). Developing a computational model based on soft tissue mechanics and bioelectric transport to estimate modulation effect changes would be highly desirable.

There are several groups that have developed sophisticated computational bioelectric models to better understand the biophysics of neuromodulation, where the models compute (a) tractography due to volume of tissue activation (VTA); and/or (b) activation of specific fiber pathways (Butson *et al* 2007, Chaturvedi *et al* 2010, Astrom *et al* 2015).

A few studies have attempted to examine and address the impact of brain shift on tractography. In Choi *et al*, shift was measured by anatomical control points using preop- and postop-imaging data in subcallosal cingulate DBS surgeries; the impact of electrode displacement was analyzed and found to alter pathway activation patterns (Choi *et al* 2018). In Horn *et al* outlining a DBS post-processing pipeline named Lead-DBS, brain shift correction capability was introduced to account for the misalignment between preop- and postop-imaging data (Horn *et al* 2019).

While these efforts to understand and/or correct for the impact of brain shift on potential treatment outcome are encouraging advances, these studies represented analyses that employed shift measurements from preop- and postop-imaging data. This study aims to advance the understanding of the effect of electrode misplacement with realistic intraoperative shift derived from the gold standard measurement provided by interventional magnetic resonance (iMR). Specifically, the impact of brain shift on functional response predicted by tractography via neural pathway recruitment is assessed. To achieve, the work presented here utilizes a multi-physics analysis framework, i.e. biomechanical and bioelectric finite element (FE) models. Subsequently this analysis framework is applied to six patients who had undergone iMR-guided DBS procedures. Based on the preliminary framework first reported in Luo *et al* (2019), the methodology in this study has been

expanded and then employed to analyze a six-case series of patients that experienced significant intraoperative brain shift during DBS implant.

The objective of this study is to provide qualitative and quantitative support linking the effects of shift-induced electrode misplacement to the degradation of targeted neural pathway recruitment. The work also provides valuable theoretical support toward a critical target deviation threshold whereby treatment quality significantly degrades. Lastly, the work establishes the potential utility and power of multi-physics modeling frameworks to help guide DBS treatments in the presence of intraoperative brain deformations.

2. Methodology

2.1. Overview

The overall analysis framework used for the study is shown in figure 1, which consists of a multi-physics patient-specific biomechanical and bioelectric FE models.

The biomechanical model (black block in figure 1) aims to provide realistic data-driven intraoperative brain shift predictions from intracranial changes in soft tissue mechanics due to burr hole and dural opening during DBS surgery. Specifically, a sparse-data constrained biomechanical model is used to estimate volumetric shift to better reflect intraoperative patient neuroanatomy. During surgery, the deployment of such model could allow for the accurate mapping of preoperative MR (pMR) targets to intraoperative physical space in the form of patient updated MR (uMR) to improve surgical navigation and targeting.

The bioelectric model (blue blocks in figure 1) aims to provide the spatial distribution of electric potential due to neuromodulation with and without shift adjustment.

Subsequently, VTA and associated neural pathway recruitment via tractography (orange block in figure 1) can be estimated and employed to establish a better understanding for functional impact of DBS therapy as well as potentially degrading events such as brain shift.

2.2. Data

The study population consists of $n = 6$ patients, who had undergone iMR-guided DBS electrode implantation through a burr hole targeting the subthalamic nucleus (STN) and experienced detectable shift observed from iMR. Imaging volumes of the patients were acquired with consent and IRB approval. The surgical details can be found in Ivan *et al* (2014). MR image specifications such as voxel spacing of imaging data (pMR and iMR) are described in Luo *et al* (2020). Briefly, pMRs and iMRs in this study were acquired using a 1.5 T MR scanner; the voxel spacing for pMR ranges from 1.00 to 2.00 mm, and for iMR ranges from 1.02 to 1.50 mm. An example of the acquired data is shown in figure 2, where brain shift due to burr hole procedure is demonstrated both on the surface as well as subsurface (indicated by corresponding crosshairs at the lateral ventricle). The imaging artifacts due to DBS electrode leads are illustrated by red arrows.

2.3. Brain shift estimation via biomechanical model

To account and estimate for shift during DBS electrode placement through a burr hole (small cranial opening), an inverse problem approach rooted in a biphasic biomechanical model was employed. This modeling approach accounts for biophysical phenomenon such as CSF drainage, gravity, pneumocephalus, and stiffness considerations of different brain components (Luo *et al* 2020). The complete work regarding the implementation details of the biomechanical modeling method such as boundary condition assignment is described in Luo *et al* (2020).

Briefly, patient pMR was utilized to construct a volumetric patient-specific FE mesh (Sullivan *et al* 1997). This mesh was then placed under varying surgical conditions, such as permutations of displacement and pressure conditions. Under each unique surgical condition, a biphasic biomechanical model was employed to compute the volumetric shift profile (Miga 1998). The collection of volumetric deformations from the distribution of boundary and forcing conditions is assembled into a 'deformation atlas' (Dumpuri *et al* 2007, Chen *et al* 2011, Narasimhan *et al* 2020). Specifically, the modeling approach leveraged here intends to capture the effect of CSF loss, gravity and pneumocephalus. In particular, the impact of CSF loss and gravity are accounted for as CSF loss reduces buoyancy, therefore introducing tissue sag. Within the aforementioned deformation atlas, different extents of CSF loss were simulated to contribute and ensure the fair distribution required to account for different intraoperative surgical conditions.

To estimate volumetric brain shift during surgery, sparse shift measurements (surface and subsurface) derived from iMR were determined by matching corresponding tissue landmarks (Luo *et al* 2020). Using these data, an inverse problem approach was employed whereby a linear combination of potential brain shift solutions is determined to best match the aforementioned measurements in a constrained least-squared error manner (Luo *et al* 2017, 2020). The model-predicted volumetric shift was then used to update pMR to better reflect intraoperative patient anatomy, as well as to estimate shift at target region for DBS therapy.

Finally, as an additional layer of rigor to the analysis, Advanced Normalization Tools (ANTs, employed as a state-of-the-art and robust nonrigid image-to-image registration utility) (Avants *et al* 2011) were utilized to co-register pMR and iMR to produce a displacement field to independently estimate deep brain target shift for a comparative evaluation to the model-based analysis (Luo *et al* 2020).

2.4. Potential distribution via bioelectric model

To compute electric potential distribution, a bioelectric FE model based on the Poisson equation using standard conductive biophysics was constructed:

$$\nabla \cdot (-\sigma \nabla V_e) = I$$

where V_e is the electric potential (Volts), σ is the conductivity tensor (S m^{-1}), and I is the injected current from a source such as an electrode contact. Here the conductivity tensor was incorporated to model tissue heterogeneity and anisotropy. To achieve, the linear relationship

described by Tuch *et al* (2001) was used that relates diffusion tensor to the electrical conductivity tensor:

$$\sigma = \frac{\sigma_e}{d_e} D$$

where σ is the electrical conductivity tensor (S m^{-1}), D is the diffusion tensor (m^2 s^{-1}), σ_e is the effective extracellular electrical conductivity (S m^{-1}), d_e is the effective extracellular diffusivity (m^2 s^{-1}) (Tuch *et al* 2001, Astrom *et al* 2012). Here in this experiment, σ_e/d_e was set to 0.844 as empirically determined by Tuch *et al* (2001). Limitations regarding this linear assumption will be further discussed later.

The performance and analysis of tractography were conducted in Montreal Neurological Institute (MNI) space (Fonov *et al* 2011). The limitation of data availability here, specifically only pMR and iMR, necessitated the need of these evaluations in MNI space, where a number of atlases are available and can be leveraged for this investigation.

To facilitate this process, essential information from previous section (shown in the top panel in figure 3, corresponding to the biomechanical modeling block in black on the left in figure 1) was transformed from patient data to MNI space. Specifically, the displacement 3D fields determined by model- and ANTs- predictions (D_{model} and D_{ANTs} in figure 3), as well as positions of DBS leads (end point and trajectory, shown as P_{ANTs} and P_{model} in figure 3) were mapped to MNI space. For the latter, briefly, the end point of the electrode path visible on iMR was determined and a second point along the electrode path (such as indicated via red arrows on figure 2) was identified to establish trajectory. The transformation of this information was achieved by registering segmented brains of patient and ICBM 152 (International Consortium for Brain Mapping) T1 weighted images (voxel spacing: 1 × 1 × 1 mm; image dimension: 193 × 229 × 193), the latter is associated with the HCP 1021 template (Human Connectome Project) available in DSI Studio (http://dsi-studio.labsolver.org/) via ANTs, shown in green arrows in figure 3 (Fonov *et al* 2011, Yeh *et al* 2013).

Once the displacement profiles were mapped to MNI space, a volumetric brain mesh reflecting the transformed model-predicted displacement profile was constructed and served as the basis of the computational domain of the bioelectric model (blue block in figure 3). In summary, as patient-specific diffusion tensor imaging (DTI) data were not available in this retrospective cohort, the process in figure 3 was specifically designed to estimate that data using an atlas DTI (HCP 1065 template, voxel spacing: 1 × 1 × 1 mm; image dimension: 182 × 218 × 182) available via FSL (Smith *et al* 2004, Woolrich *et al* 2009, Jenkinson *et al* 2012, Glasser *et al* 2013, Sotiropoulos *et al* 2013).

Once mapped, the effects of anisotropic and heterogenous conductive modeling environments are incorporated. While a limitation, as utilization of the atlas does not allow for a patient-specific assessment of change, this does allow for a realistic and reasonable approximation of that change.

To complete the computational domain, DBS leads were reconstructed: the transformed end point and trajectory (P_{ANTs} and P_{model}) were used in addition to the known manufacturer specifications of Medtronic 3389 (Medtronic Inc., Minneapolis, MN, USA). DBS electrodes were reconstructed and incorporated into the model above. In addition, to account for tissue encapsulation effect, another sub-domain around the electrode contact with the thickness of 0.5 mm was introduced and assigned a conductivity of 0.1 S m^{-1} (Butson *et al* 2006, Butson and McIntyre 2008). For mesh generation, a Free Tetrahedral operation was performed using COMSOL Multiphysics (version. 5.4, COMSOL AB, Stockholm, Sweden). Specifically, the element size for the brain domain was calibrated for general physics with predefined size of normal; electrode contacts and the encapsulation layer were given the element size of extra fine. Furthermore, an additional mesh refinement was performed for the domains around electrode contacts where the number of refinements was set to two. The node number for the 18 meshes generated (two deformation possibilities and one undeformed state for six patients) is ~66 654 ± 12 991.

An example of the constructed bioelectric FE mesh model representing deformed patient anatomy (with asymmetric shift in the left frontal lobe) with reconstructed electrode leads (active contact 1 is shown as red and other contacts are shown in black) is demonstrated in figure 4 and is represented in the blue block in figures 1 and 3.

Lastly, with transformed displacement profiles via model and ANTs, locations of reconstructed electrode leads could be adjusted accordingly within the bioelectric model for simulation.

2.5. VTA and tractography

To better understand the bioelectrical behavior near the electrode contacts, a regular grid of 20 × 20 × 20 mm (Anderson *et al* 2018, 2019) was defined with the active contact (here contact 1 was active while the brain surface served as the ground) as the centroid. Along each dimension of the grid, 200 evenly distributed grid points were examined for a total of 8 000 000 points. The stimulation configuration in this study was monopolar current stimulation at 3 mA (Butson and McIntyre 2005a). The electric potential profile from the bioelectric model was then used to estimate the VTA, which was based on an isolevel of 0.2 V mm^{-1} (Astrom *et al* 2015, Alonso *et al* 2018). Subsequently deterministic tractography as well as fiber trimming were performed in DSI Studio (Yeh *et al* 2013) with the estimated VTA as the region of interest (ROI). Here the parameters used were default quantitative anisotropy (qa) threshold, angular threshold of 60°, step size 0.5 mm, smoothing parameter 0.2, length 20.0–200.0 mm, and fiber count of 5000 with an additional termination consideration of seed count of 500 000 (Yeh *et al* 2013, Luo *et al* 2019).

The estimation of VTA and tractography were completed in three different configurations of lead reconstructions as noted in the previous section: without shift consideration, with shift consideration via model prediction, and with shift consideration via ANTs prediction.

2.6. Assessing shift impact on neural pathway

Once tractography was estimated in each of the three configurations described in the previous section, tract volume outputted by DSI Studio was directly compared as well as in terms of relative percent change in an effort to assess the differences due to brain shift.

Furthermore, to probe potential impacts on motor functions, volumetric overlap between predicted fiber bundles and regions associated with motor functions (i.e. precentral and postcentral gyri, available through AAL2 (Rolls *et al* 2015) provided in DSI Studio) was computed. The differences due to brain shift were calculated using the configuration of without shift as the baseline and were related to estimated shift measurements.

Connectivity matrix was obtained using the parcellation atlas of AAL2 (Rolls *et al* 2015) counting the number of tracts that end in defined regions with the default threshold. Using the connectivity profile without shift consideration as the baseline, comparative changes in each shift-considered connectivity matrix were calculated and further examined.

In order to correlate target region shift or bulk tissue movement at deep brain target reported in Luo *et al* (2020) with changes in neural pathway prediction, the fiber bundles were converted into a binary mask image and transformed to patient space. To compute the similarity between two fiber bundles, specifically with and without shift consideration (recall for comparison, shift consideration is provided via two configurations: model prediction or ANTs prediction), the Jaccard index (Kosub 2019), or Intersection over Union (IoU), was used as a metric. Jaccard index is defined as follows (Kosub 2019):

$$J(A, B) = \text{def} \frac{|A \cap B|}{|A \cup B|}$$

where A and B are two finite sets, or here the mask images representing the predicted fiber bundles of interest, and J is the Jaccard index. In this study, the Jaccard index is also referred to as the volumetric overlap as it measures similarity between two sets of fiber bundle of interest: ranging from 0 to 100%, higher percentage presents a greater degree of similarity between two sets. It should be noted that while metrics were examined within the context of each shift prediction method, i.e. model and ANTs, the results were also combined to assess the overall impact of reasonable shift estimations provided by two distinct methods.

3. Results

3.1. Estimated shift at deep brain target

Estimated brain shifts using the biophysics-based model approach and ANTs are reproduced from Luo *et al* (2020) in table 1. The results in table 1 represent an understanding of bulk tissue movement at deep brain target region and are leveraged later as a variable in the correlation study where the impact of brain shift on recruited pathway is assessed.

Overall, the average bulk tissue movement at deep brain target region predicted by the model is 1.2 ± 0.9 mm and ANTs is 1.4 ± 0.7 mm. The findings in Luo *et al* (2020) stated that with respect to model and ANT prediction comparisons in areas with high feature image contrast,

ANTs outperformed the model-based approach at designated tissue feature targets. However, this result was expected given the distinct difference in the density of data driving the two registration methods (i.e. ANTs uses full volumetric intensity data, while the model uses a sparse set of surface and subsurface points). With respect to deep brain targets, the improved performance was not nearly as certain as tissue feature intensity contrast is not as profound (Luo *et al* 2020). Nevertheless, despite differences, the previous study revealed that each provided a viable shift at the deep brain target region, which provides credence to estimating the impact of these shifts on neural pathway recruitment analyzed herein.

3.2. VTA estimation

VTA estimation (in purple) is illustrated in figure 5, using contact 1 shown in red superimposed with patient MR in the HCP 1021 template space with zoomed perspective.

3.3. Tractography prediction

An example of predicted tractography due to estimated VTAs resulted from activation of both implants is shown in figure 6(a). An example of the difference in predicted tractography due to different reconstructed DBS leads as a result of shift consideration is shown in figure 6(b), where blue represents tractography due to reconstructed electrode leads without shift consideration, and red represents leads with model-predicted shift consideration.

An examination of tract volume outputted by DSI Studio illustrates the potential impact of shift, which is reported in table 2 (columns 2 and 3). Furthermore, percent change from shift-considered tracts to their counterparts without shift consideration was computed, shown in table 2 (columns 4 and 5).

Analyzing changes in tract volume further, figure 7(a) demonstrates its strong relation with estimated shift: (a) Pearson correlation coefficient (CC) was computed where $R = 0.70$, 0.83 and 0.67 for absolute difference in tract volume for model prediction, ANTs prediction, and combined data, respectively; (b) for thoroughness, similarly Spearman's rank CC was also computed where $\rho = 0.91$, 0.60 and 0.80, respectively for model, ANTs, and combined data, thus both indicating the strong correlative impact of shift.

Since one objective of this study is to assess a possible threshold where tractography output (e.g. tract volume) may be impacted considerably by brain shift, here the combined data points in figure 7(a) were partitioned into two regions to determine such delineation. Specifically, the data points were divided into two cluster regions via k-means, shown in figure 7(b) in pink and blue; interestingly the partition occurred as shift approached ~2 mm and change in volume approached ~2485 mm^3.

In addition to tract volume, the volumetric overlap between predicted fiber bundles and regions associated with motor functions, specifically precentral (in orange) and postcentral gyri (in cyan) shown in figure 8(a), was examined. Here the absolute difference in volumetric overlap of two different configurations (no shift vs. model-predicted shift, and no shift vs. ANTs-predicted shift) were computed and summarized in table 3. Figure 8(b) correlates the combined data of the absolute differences in motor ROI volumetric overlap

with estimate target shift in table 1. The results suggest the correlative impact of shift on change of fiber bundles' overlap associated with motor regions (via Pearson CC as R = 0.53).

3.4. Volumetric overlap (Jaccard index)

For each patient, the recruited pathway due to implants without shift consideration and its counterpart with shift consideration (model or ANTs) are compared for similarity via the Jaccard index or volumetric overlap. Here, when comparing two fiber bundles/sets in table 4, the combined set of two bundles is considered at 100%, and (a) the subset that is unique to the pathway from without shift consideration is labeled as 'Unshifted-unique volume fraction' in table 4. (b) Similarly, the subset that is unique to the pathway with shift consideration is labeled as 'Shifted-unique volume fraction.' (c) Lastly, the shared component of the two sets is labeled as 'Volumetric overlap,' effectively representing the Jaccard index. This relationship of the three components of interest is further illustrated in the Venn diagram in table 4.

Results for each patient are summarize in table 4, where volumetric overlap (Jaccard index) is shown in column 5 (model) and column 8 (ANTs), recall differences in displacement profile for model and ANTs predictions. Moreover, the volumetric overlap is plotted with corresponding shift estimation in figure 9. A linear regression was performed with Pearson CC (in figure 9), with model-prediction (red) and ANTs-prediction (blue) separately considered, as well as together.

Here the Pearson CCs were $R = -0.88$, -0.78 and -0.83 for volumetric overlap resulted from model-prediction, ANTs prediction and combined data, respectively. Moreover, the thresholds at which the estimated volumetric overlap became 0%, i.e. the inverse of the slope in the linear regression shown in figure 9 are 3.02, 2.87, and 2.94 mm, respectively for model-prediction, ANTs prediction and combined data.

3.5. Connectivity profile

Using the multi-physics models and fiber tract recruitment strategies in the previous sections, a connectivity matrix can be determined via DSI Studio with respect to precentral and postcentral gyri, considered to contribute to motor response in DBS (Accolla *et al* 2016, Younce *et al* 2019). Structural connectivity change within the context of model- and ANTs-based predictions was computed. This connectivity profile that represents *changes* from baseline to its shifted counterpart normalized in a connecto-gram (Kassebaum 2020) is illustrated in figure 10. The width of the line represents the strength of change. The details describing regions in the parcellation atlas of AAL2 in figure 10 can be found in Rolls *et al* (2015).

4. Discussion

An analysis on the impact of intraoperative brain shift, derived from pMR and iMR imaging data, on fiber tract recruitment was conducted using a multi-physics FE modeling approach. When this framework was applied to six patients with pMR and iMR data, a critical threshold was characterized where deviation from the intended target could

potentially result in sharp decreases in efficacy. It was determined that a strong linear relation exists between the deviation from intended target and changes in intended neural pathway activation with Pearson CC of −0.83. With respect to the degradation of activation, figure 9 predicts that at a target error of ~2.94 mm, all intended activation would be affected. This threshold, determined via realistic shift estimated from two different shift prediction methods (biophysics-modeling and ANTs), provides quantitative evidence supporting previous observations that deviation/misplacement of ~2–3 mm may introduce inadequate treatment or poor outcome. While these conventional thresholds have been noted, to our knowledge the linear relationship found in figure 9 is quite profound in that it estimates an approximate 34% degradation in intended intentional functional activation per 1 mm of targeting error in electrode positioning. It should also be noted that in data not reported here, activation of remaining contacts (i.e. contacts 0, 2 and 3) were also examined and yielded similar trends to that of contact 1. As a comparator, equivalent Pearson CCs of active −0.82, −0.92 and −0.94 were calculated for active contacts 0, 2 and 3, respectively. In addition, the estimated threshold at which intended activation degrades to 0%, was 3.10, 2.75 and 2.61 mm for active contacts 0, 2 and 3, respectively. Given limitations and errors associated with data processing and modeling that will be discussed later, this estimation ranging from 2.61 to 3.10 mm at which intended neural pathway recruitment is lost is remarkably consistent with experiences in the literature. For example, in Kremer *et al*, an intraoperative CT (iCT) system was employed to verify lead placement, lead repositioning was deemed necessary if misplacement error of greater than 2 mm from intended target was detected (Kremer *et al* 2019).

In addition to the volumetric overlap metric, it is important to note the changes induced by brain shift on other metrics: (a) for tract volume in table 2, the average relative change of tract volume can be up to 33.2%. Furthermore, when correlation between absolute difference in volume and estimated deep brain target region shift was examined among conditions without and with shift considerations, correlative impact of shift on tract volume was observed and is shown in figure 7. For tract volume, specifically for Pearson CC, $R = 0.67$ for the combined data points and for Spearman's rank CC, $\rho = 0.80$. (b) For overlapping volume with motor regions in table 3, correlative impact of shift on changes of the overlapping volume was examined and a moderate Pearson CC of $R = 0.53$ was determined in figure 8. (c) Moreover, figure 10 illustrates the changes in connectivity profile due to shift (model and ANTs) with respect to precentral and postcentral gyri. A notable connection alteration between configurations with and without shift consideration is the cerebellum. Recent studies have shown that in addition to basal ganglia (including STN), cerebellum may have functional implications on pathophysiology of PD such as motor learning (Wu and Hallett 2013, Sweet *et al* 2014, Marcelino *et al* 2019). Such connectivity alteration to cerebellum with its potential therapeutic implications further illustrate the need to account for brain shift in electrode placement and stimulation.

However, it is important to note several limitations of the study. First, additional considerations for stimulation modeling are desired. While considering nature of the medium with current or voltage input, the model here only evaluates purely conductive medium without considering frequency-dependency of both the capacitive effects in the medium and stimulus waveform utilized clinically. As noted by Butson *et al*, the approach

taken here may overestimate VTA where error may be attributed to stimulation pulse width and electrode capacitance (Butson and McIntyre 2005b). Fourier FEM (finite element modeling) should be considered in the future to account for frequency-dependence of stimulus waveform as well as capacitive effects of the computational medium (Butson and McIntyre 2005b, Howell and McIntyre 2016). Lastly, we would like to acknowledge that the simple linear relation used for obtaining conductivity properties from diffusion tensor can be improved. Studies (Wu *et al* 2018, Nordin *et al* 2021) have observed some impacts/deficiencies in the relation derived by Tuch *et al* (2001): e.g. Wu *et al* (2018) noted that it is based on effective medium theory and does not directly and adequately account for the impact of the structures and natures of the brain tissues. Therefore, more sophisticated methods such as in Schmidt and Rienen (2012) and Howell and McIntyre (2016) relating diffusion tensor to the conductivity tensor can further improve and refine the establishment of the anisotropic and heterogenous medium. Nevertheless, while important, as the purpose of this study was to demonstrate relative changes, the work reported has considerable independent value.

A second limitation is with respect to the estimation of VTA. A number of methods reviewed in Gunalan *et al* have been proposed to obtain VTA or to estimate neural responses due to stimulation (Gunalan *et al* 2018). The VTA estimation similar to Astrom *et al* (2015) and (2018) was selected here for its computational efficiency in this initial analysis. However, it is recognized that VTA-based method has limitations noted by Gunalan *et al* (2018), particularly with bipolar and multipolar stimulation conditions (Duffley *et al* 2019). Field-cable (FC) model, i.e. multi-compartment cable models of axons in the NEURON modeling environment, considered the gold standard, would provide better estimation of neural activation (McNeal 1976, McIntyre and Foutz 2013, Sweet *et al* 2016, Howell and McIntyre 2016, Gunalan *et al* 2018, McIntyre 2018). In particular, impact and sensitivity of fiber orientation on functional outcome of DBS therapy could be further considered, similar to in Lehto *et al* (2017) and Slopsema *et al* (2021) where functional MRI (fMRI) was leveraged. The approach of leveraging NEURON modeling environment as well as accounting for fiber orientation where pathway activation percentage can be assessed should be a part of further retrospective analysis on the impact of shift on neural pathway recruitment (Lehto *et al* 2017, Gunalan *et al* 2018, Anderson *et al* 2019, Duffley *et al* 2019, Slopsema *et al* 2021).

Another limitation of the study is the lack of patient-specific diffusion weighted imaging (DWI) data, which necessitated a number of registrations performed here to the population-averaged template space (indicated by the green arrows in figure 3), which could contribute to potential registration bias. Specifically, given the pathology of the patients in this study, they may deviate from healthy DWI on a patient level due to possible atrophy from disease duration. However, a recent report examined the connectivity analysis via patient specific information vs. normative atlases, the latter being the approach taken in this work, and found that while not interchangeable, the connectivity profiles produced by each method can yield similar conclusions with respect to clinical outcome (Wang *et al* 2020). This does provide some credence to the overall conclusions drawn in this study with the use of the population-averaged template. Nevertheless, this comparison report described above (Wang *et al* 2020) does note that, while results are not statistically significant, patient-specific

information may lead to slightly better prediction of clinical outcomes. Therefore, future work will involve the acquisition of patient-specific DWI and conduct a similar comparison study to extend the findings of this study.

Moreover, for future directions, there are two possibilities to consider: (a) for shift assessment, a better understanding with final lead position via postop imaging data could provide further data points, in addition to intraoperative brain shift, of the impact of shift on clinical outcome in a longitudinal manner, similar to a promising study recently conducted by (Goransson *et al* 2020); (b) clinical effects, instead of simulated tractography, would be preferred and desired.

Despite the limitations outlined above, the experimental design reported provides a consistent and identical modeling environment for all simulations within this comparison study. In this context, similar estimation errors and limitations (i.e. registration, localization, shift measurements, etc) are present and expected among all groups; thus, the overall conclusions regarding the impact of brain shift on neural pathway recruitment, while not absolute, do become informative rather than definitive.

5. Conclusion

A retrospective analysis was performed to assess the impact of brain shift on DBS functional outcome as evaluated by tractography. The analysis leverages a multi-physics biomechanical and bioelectric modeling framework. The former provides realistic intraoperative brain shift estimation, and the latter is used to predict electric potential. The potential solution profile is subsequently used to estimate VTA and predict the recruitment of neural pathways. With the application of this analysis framework to the preop- and intraop-imaging data of six patients, shift consideration at deep brain target region is demonstrated to introduce differences in tract volume, motor ROI volumetric overlap, as well as connectivity profile. A strongly negative correlation is found between deviation from intended target and recruitment of neural pathways, where a threshold average of ~2.85 mm across all lead electrodes is determined to critically degrade intended neural pathway recruitment. In addition, an estimate of the rate of intended neural pathway recruitment degradation as a function of target error was determined, i.e. an approximate 34% degradation in neural recruitment for every 1 mm in electrode positioning error. This finding provides quantitative evidence to support literature reports that deviations of 2–3 mm from intended target produces poor or inadequate clinical outcomes. This is important as such deviations can result in lead position revision or removal altogether. Finally, while the framework provided has served as an analysis tool for data taken intraoperatively, the fidelity of the results does provide an exciting prospect for the use of multi-physics models as an inexpensive planning, guidance, and delivery platform for DBS therapy.

Acknowledgments

This work is supported by the National Institute for Neurological Disorders and Stroke, of the National Institutes of Health, R01NS049251.

Data availability statement

The data generated and/or analysed during the current study are not publicly available for legal/ethical reasons but are available from the corresponding author on reasonable request.

References

Accolla EA, Ruiz MH, Horn A, Schneider GH, Schmitz-Hubsch T, Draganski B and Kuhn AA 2016 Brain networks modulated by subthalamic nucleus deep brain stimulation Brain 139 2503–15 [PubMed: 27412387]

Alonso F, Vogel D, Johansson J, Wardell K and Hemm S 2018 Electric field comparison between microelectrode recording and deep brain stimulation systemsa simulation study Brain Sci. 8 15

Anderson DN, Duffley G, Vorwerk J, Dorval AD and Butson CR 2019 Anodic stimulation misunderstood: preferential activation of fiber orientations with anodic waveforms in deep brain stimulation J. Neural Eng 16 11

Anderson DN, Osting B, Vorwerk J, Dorval AD and Butson CR 2018 Optimized programming algorithm for cylindrical and directional deep brain stimulation electrodes J. Neural Eng 15 18

Astrom M, Diczfalusy E, Martens H and Wardell K 2015 Relationship between neural activation and electric field distribution during deep brain stimulation IEEE Trans. Biomed. Eng 62 664–72 [PubMed: 25350910]

Astrom M, Lemaire JJ and Wardell K 2012 Influence of heterogeneous and anisotropic tissue conductivity on electric field distribution in deep brain stimulation Med. Biol. Eng. Comput 50 23–32 [PubMed: 22101515]

Avants BB, Tustison NJ, Song G, Cook PA, Klein A and Gee JC 2011 A reproducible evaluation of ANTs similarity metric performance in brain image registration Neuroimage 54 2033–44 [PubMed: 20851191]

Balachandran R, Mitchell JE, Dawant BM and Fitzpatrick JM 2009 Accuracy evaluation of microtargeting platforms for deep-brain stimulation using virtual targets IEEE Trans. Biomed. Eng 56 37–44 [PubMed: 19224717]

Bratsos SP, Karponis D and Saleh SN 2018 Efficacy and safety of deep brain stimulation in the treatment of parkinson's disease: a systematic review and meta-analysis of randomized controlled trials Cureus 10 20

Butson CR, Cooper SE, Henderson JM and McIntyre CC 2007 Patient-speciftic analysis of the volume of tissue activated during deep brain stimulation Neuroimage 34 661–70 [PubMed: 17113789]

Butson CR, Maks CB and McIntyre CC 2006 Sources and effects of electrode impedance during deep brain stimulation Clin. Neurophysiol 117 447–54 [PubMed: 16376143]

Butson CR and McIntyre CC 2005a Tissue and electrode capacitance reduce neural activation volumes during deep brain stimulation Clin. Neurophysiol 116 2490–500 [PubMed: 16125463]

Butson CR and McIntyre CC 2008 Current steering to control the volume of tissue activated during deep brain stimulation Brain Stimul. 1 7–15 [PubMed: 19142235]

Butson CR and McIntyre CC and IEEE 2005b 2nd Int. IEEE/EMBS Conf. on Neural Engineering (Arlington, VA, 16–20 March 2005) vol Series (New York: IEEE) pp 196–7

Chaturvedi A, Butson CR, Lempka SF, Cooper SE and McIntyre CC 2010 Patient-specific models of deep brain stimulation: influence of field model complexity on neural activation predictions Brain Stimul. 3 65–77 [PubMed: 20607090]

Chen I, Coffey AM, Ding S, Dumpuri P, Dawant BM, Thompson RC and Miga MI 2011 Intraoperative brain shift compensation: accounting for dural septa IEEE Trans. Biomed. Eng 58 499–508 [PubMed: 21097376]

Choi KS, Noecker AM, Riva-Posse P, Rajendra JK, Gross RE, Mayberg HS and McIntyre CC 2018 Impact of brain shift on subcallosal cingulate deep brain stimulation Brain Stimul. 11 445–53 [PubMed: 29246748]

Collins KL, Lehmann EM and Patil PG 2010 Deep brain stimulation for movement disorders Neurobiol. Dis 38 338–45 [PubMed: 19969083]

Duffley G, Anderson DN, Vorwerk J, Dorval AD and Butson CR 2019 Evaluation of methodologies for computing the deep brain stimulation volume of tissue activated J. Neural Eng 16 15

Dumpuri P, Thompson RC, Dawant BM, Cao A and Miga MI 2007 An atlas-based method to compensate for brain shift: preliminary results Med. Image Anal 11 128–45 [PubMed: 17336133]

Elias WJ, Fu KM and Frysinger RC 2007 Cortical and subcortical brain shift during stereotactic procedures J. Neurosurg 107 983–8 [PubMed: 17977271]

Fonov V, Evans AC, Botteron K, Almli CR, McKinstry RC, Collins DL and Brain Dev Cooperative G 2011 Unbiased average age-appropriate atlases for pediatric studies Neuroimage 54 313–27 [PubMed: 20656036]

Glasser MF et al. 2013 The minimal preprocessing pipelines for the human connectome project Neuroimage 80 105–24 [PubMed: 23668970]

Goransson N, Johansson JD, Wardell K and Zsigmond P 2020 Postoperative lead movement after deep brain stimulation surgery and the change of stimulation volume Stereotact. Funct. Neurosurg 9

Gunalan K, Howell B and McIntyre CC 2018 Quantifying axonal responses in patient-specific models of subthalamic deep brain stimulation Neuroimage 172 263–77 [PubMed: 29331449]

Horn A et al. 2019 Lead-DBS v2: towards a comprehensive pipeline for deep brain stimulation imaging Neuroimage 184 293–316 [PubMed: 30179717]

Howell B and McIntyre CC 2016 Analyzing the tradeoff between electrical complexity and accuracy in patient-specific computational models of deep brain stimulation J. Neural Eng 13 036023 [PubMed: 27172137]

Ivan ME, Yarlagadda J, Saxena AP, Martin AJ, Starr PA, Sootsman WK and Larson PS 2014 Brain shift during bur hole-based procedures using interventional MRI J. Neurosurg 121 149–60 [PubMed: 24785326]

Jenkinson M, Beckmann CF, Behrens TE, Woolrich MW and Smith SM 2012 FSL Neuroimage 62 782–90 [PubMed: 21979382]

Kassebaum P circularGraph GitHub (available at: www.github.com/paul-kassebaum-mathworks/circularGraph) (Accessed 22 March 2020)

Kosub S 2019 A note on the triangle inequality for the Jaccard distance Pattern Recognit. Lett 120 36–38

Kremer NI, Oterdoom DLM, Van Laar PJ, Pina-Fuentes D, Van Laar T, Drost G, Van Hulzen ALJ and Van Dijk JMC 2019 Accuracy of intraoperative computed tomography in deep brain stimulation—a prospective noninferiority study Neuromodulation 22 472–7 [PubMed: 30629330]

Lehto LJ et al. 2017 Orientation selective deep brain stimulation J. Neural Eng 14 9

Luo M, Frisken SF, Weis JA, Clements LW, Unadkat P, Thompson RC, Golby AJ and Miga MI 2017 Retrospective study comparing model-based deformation correction to intraoperative magnetic resonance imaging for image-guided neurosurgery J. Med. Imaging 4 16

Luo M, Larson PS, Martin AJ, Konrad PE and Miga MI 2019 Medical Image Computing and Computer Assisted Intervention—MICCAI 2019 vol Series (Cham: Springer International Publishing) pp 682–90

Luo M, Larson PS, Martin A and Miga MI 2020 Accounting for deformation in deep brain stimulation surgery with models: comparison to interventional magnetic resonance imaging IEEE Trans. Biomed. Eng 67 2934–44 [PubMed: 32078527]

Marcelino ALD, Horn A, Krause P, Kuhn AA and Neumann WJ 2019 Subthalamic neuromodulation improves short-term motor learning in Parkinson's disease Brain 142 2198–206 [PubMed: 31169872]

McClelland S, Ford B, Senatus PB, Winfield LM, Du YE, Pullman SL, Yu Q, Frucht SJ, McKhann GM and Goodman RR 2005 Subthalamic stimulation for Parkinson disease: determination of electrode location necessary for clinical efficacy Neurosurg. Focus 19 E12

McIntyre CC 2018 Neuromodulation Second ed Krames ES et al. (New York: Academic) pp 129–35

McIntyre CC and Foutz TJ 2013 Computational modeling of deep brain stimulation Handb. Clin. Neurol 116 55–61 [PubMed: 24112884]

McNeal DR 1976 Analysis of a model for excitation of myelinated nerve IEEE Trans. Biomed. Eng 23 329–37 [PubMed: 1278925]

Miga MI 1998 Development and quantification of a 3D brain deformation model for model-updated image-guided stereotactic neurosurgery Engineering (Hanover, NH: Dartmouth College) 64–81

Narasimhan S, Weis J, Luo M, Simpson A, Thompson R and Miga M 2020 Accounting for intraoperative brain shift ascribable to cavity collapse during intracranial tumor resection J. Med. Imaging 7 031506

Nordin T, Wårdell K and Johansson JD 2021 8th European Medical and Biological Engineering Conf. (Cham) vol Series ed Jarm T et al. (Springer International Publishing) pp 1069–77

Rolls ET, Joliot M and Tzourio-Mazoyer N 2015 Implementation of a new parcellation of the orbitofrontal cortex in the automated anatomical labeling atlas Neuroimage 122 1–5 [PubMed: 26241684]

Rolston JD, Englot DJ, Starr PA and Larson PS 2016 An unexpectedly high rate of revisions and removals in deep brain stimulation surgery: analysis of multiple databases Parkinsonism Relat. Disord 33 72–7 [PubMed: 27645504]

Schmidt C and Rienen UV 2012 Modeling the field distribution in deep brain stimulation: the influence of anisotropy of brain tissue IEEE Trans. Biomed. Eng 59 1583–92 [PubMed: 22410323]

Slopsema JP et al. 2021 Orientation-selective and directional deep brain stimulation in swine assessed by functional MRI at 3T Neuroimage 224 9

Smith SM et al. 2004 Advances in functional and structural MR image analysis and implementation as FSL Neuroimage 23 S208–S19 [PubMed: 15501092]

Sotiropoulos SN et al. 2013 Advances in diffusion MRI acquisition and processing in the human connectome project Neuroimage 80 125–43 [PubMed: 23702418]

Sullivan JM, Charron G and Paulsen KD 1997 A three-dimensional mesh generator for arbitrary multiple material domains Finite Elem. Anal. Des 25 219–41

Sweet JA, Pace J, Girgis F and Miller JP 2016 Computational modeling and neuroimaging techniques for targeting during deep brain stimulation Front. Neuroanat 10 16 [PubMed: 26941614]

Sweet JA, Walter BL, Gunalan K, Chaturvedi A, McIntyre CC and Miller JP 2014 Fiber tractography of the axonal pathways linking the basal ganglia and cerebellum in Parkinson disease: implications for targeting in deep brain stimulation J. Neurosurg 120 988–96 [PubMed: 24484226]

Tuch DS, Wedeen VJ, Dale AM, George JS and Belliveau JW 2001 Conductivity tensor mapping of the human brain using diffusion tensor MRI Proc. Natl Acad. Sci. USA 98 11697–701 [PubMed: 11573005]

Wang Q et al. 2020 Normative vs. patient-specific brain connectivity in deep brain stimulation Neuroimage 224 117307 [PubMed: 32861787]

Woolrich MW, Jbabdi S, Patenaude B, Chappell M, Makni S, Behrens T, Beckmann C, Jenkinson M and Smith SM 2009 Bayesian analysis of neuroimaging data in FSL Neuroimage 45 S173–86 [PubMed: 19059349]

Wu T and Hallett M 2013 The cerebellum in Parkinson’s disease Brain 136 696–709 [PubMed: 23404337]

Wu ZX, Liu Y, Hong M and Yu XH 2018 A review of anisotropic conductivity models of brain white matter based on diffusion tensor imaging Med. Biol. Eng. Comput 56 1325–32 [PubMed: 29855784]

Yeh FC, Verstynen TD, Wang YB, Fernandez-Miranda JC and Tseng WYI 2013 Deterministic diffusion fiber tracking improved by quantitative anisotropy PLoS One 8 16

Younce JR, Campbell MC, Perlmutter JS and Norris SA 2019 Thalamic and ventricular volumes predict motor response to deep brain stimulation for Parkinson’s disease Parkinsonism Relat. Disord 61 64–69 [PubMed: 30527905]

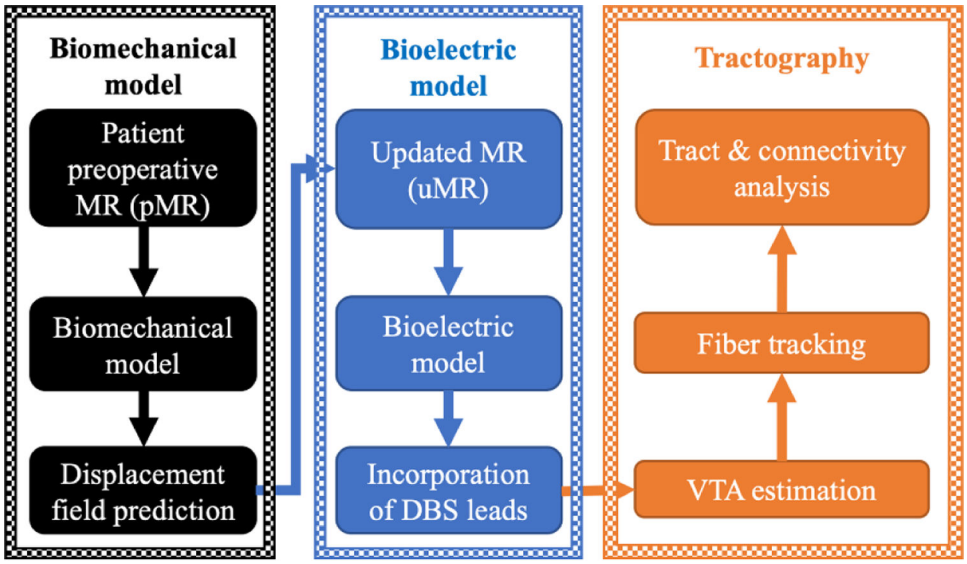

Figure 1.

A predictive multi-physics FE modeling framework for brain shift prediction via biomechanical model (left—black block), electric potential computation via bioelectric model (middle—blue block), with subsequent analysis of VTA estimation and tractography (right—orange block).

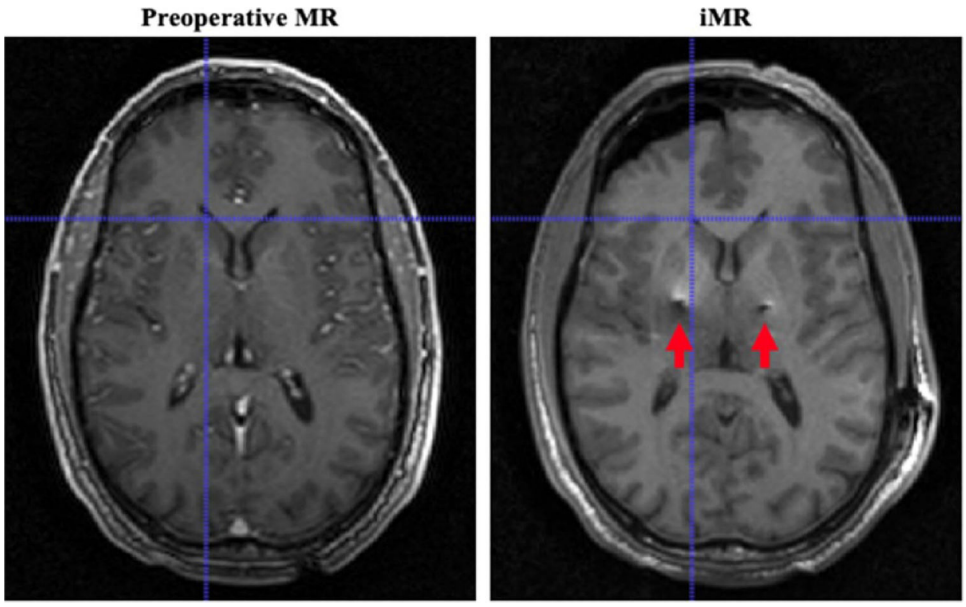

Figure 2.

An example of imaging data in this study: demonstration of the impact of brain shift during DBS burr hole surgery on the surface as well as subsurface (corresponding crosshairs at the lateral ventricle). Red arrows indicate the imaging artifacts resulted from implanted electrode leads.

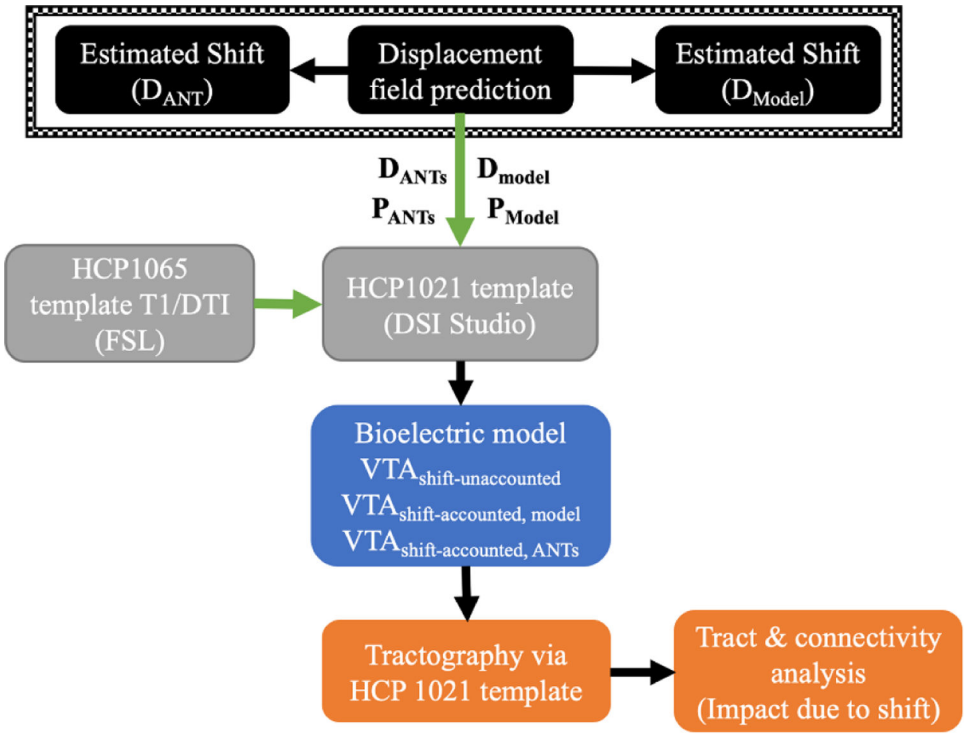

Figure 3.

A flowchart of the study: accounting for different shift considerations (model- and ANTs- predictions in black block) within the bioelectric model (blue block) for VTA estimations in HCP 1021 template (grey block), for subsequent examination of tractography (orange block). Overall analysis and modeling are performed in MNI space achieved by co-registration of T1 weighted images via ANTs (represented in green arrows).

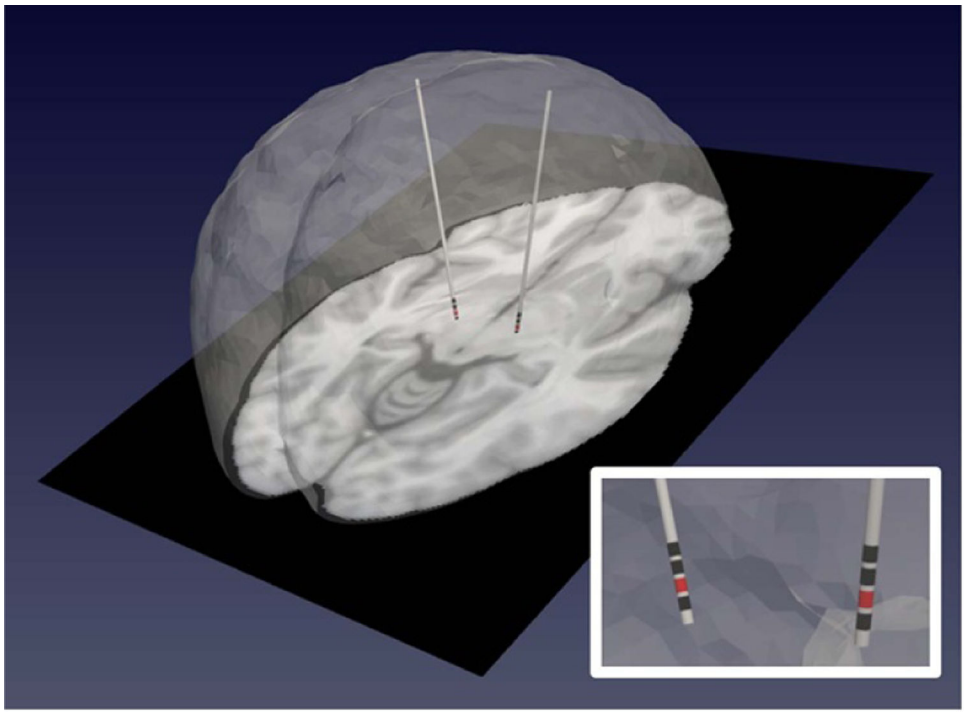

Figure 4.

A patient-specific bioelectric model representing deformed patient anatomy (noting asymmetric shift in the left frontal lobe) with reconstructed electrode leads incorporated. Contact 1 is shown as the active contact in red, while other contacts are shown in black.

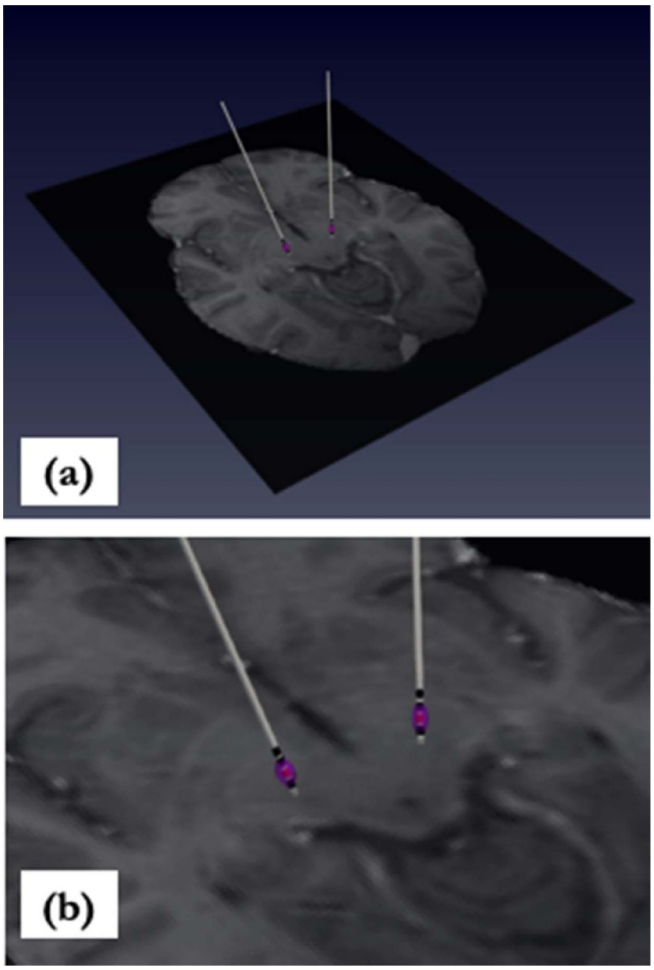

Figure 5.
(a) VTA estimation (purple) superimposed with patient MR in HCP 1021 template space. VTA is due to activation of contact 1 (shown in red). (b) Zoomed perspective.

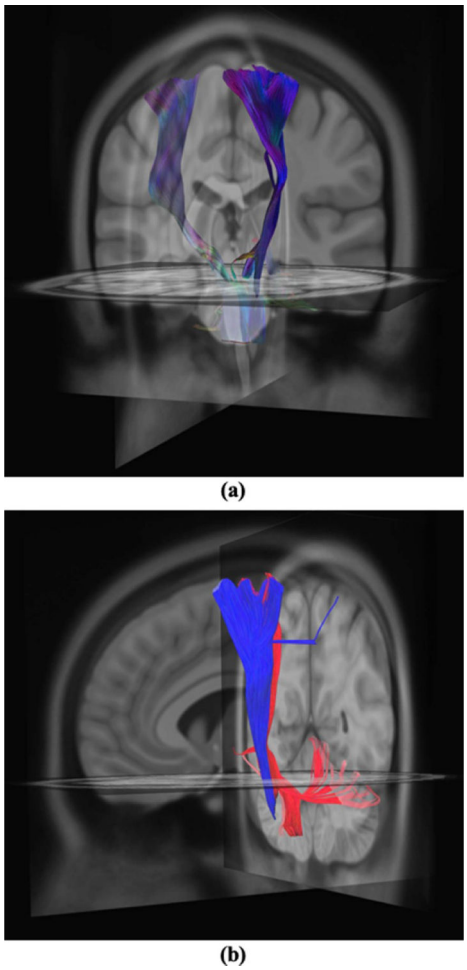

Figure 6.

(a) Predicted tractography due to estimated VTAs from neuromodulation of left and right implants. (b) Comparison of tracts without shift consideration (red) and with model-predicted shift consideration (blue).

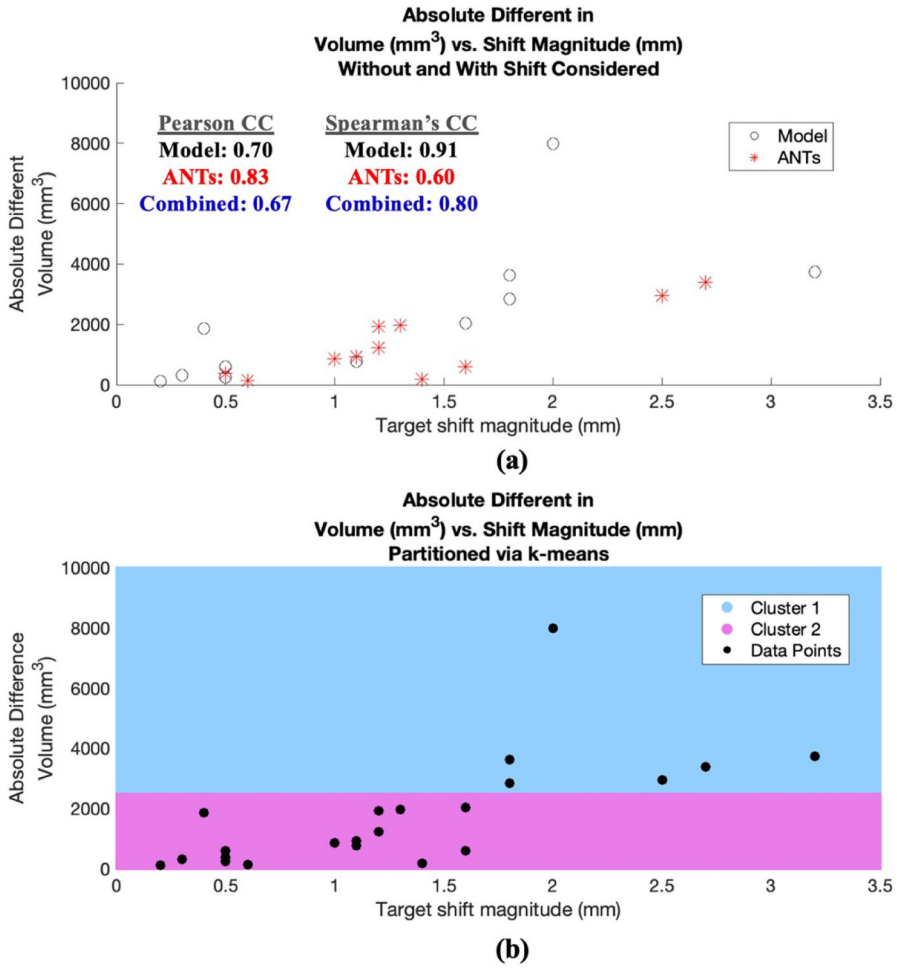

Figure 7.

Absolute difference in tract volume vs. estimated shift at deep brain target region. (a) Data points associated with model prediction shown in black and ANTs in red. Pearson and Spearman's CCs for configurations of model, ANTs, and combined data are also shown, all indicting the impact of shift on tract statistics from baseline without shift consideration. (b) The same data points in (a) are partitioned into two cluster regions via k-means shown in blue and pink, indicating two distinct clusters as shift approaches ~2 mm and change in volume approaches ~2485 mm^3.

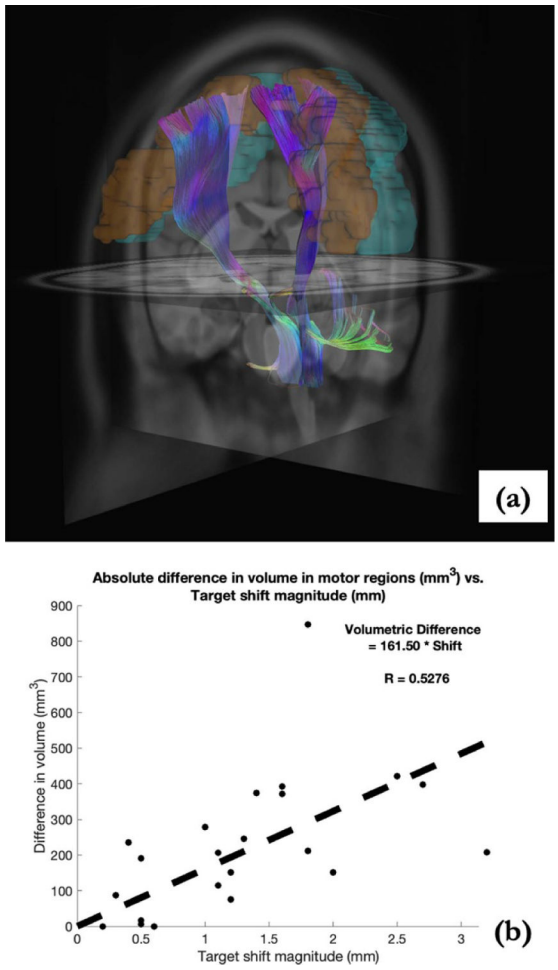

Figure 8.

(a) Predicted fiber tracts shown with precentral (orange) and postcentral (cyan) gyri. (b) Absolute change in volumetric overlap with motor regions (no-shift consideration as the baseline) analyzed with estimated shift at target region, suggesting the impact of brain shift, i.e. deviation from surgical plan.

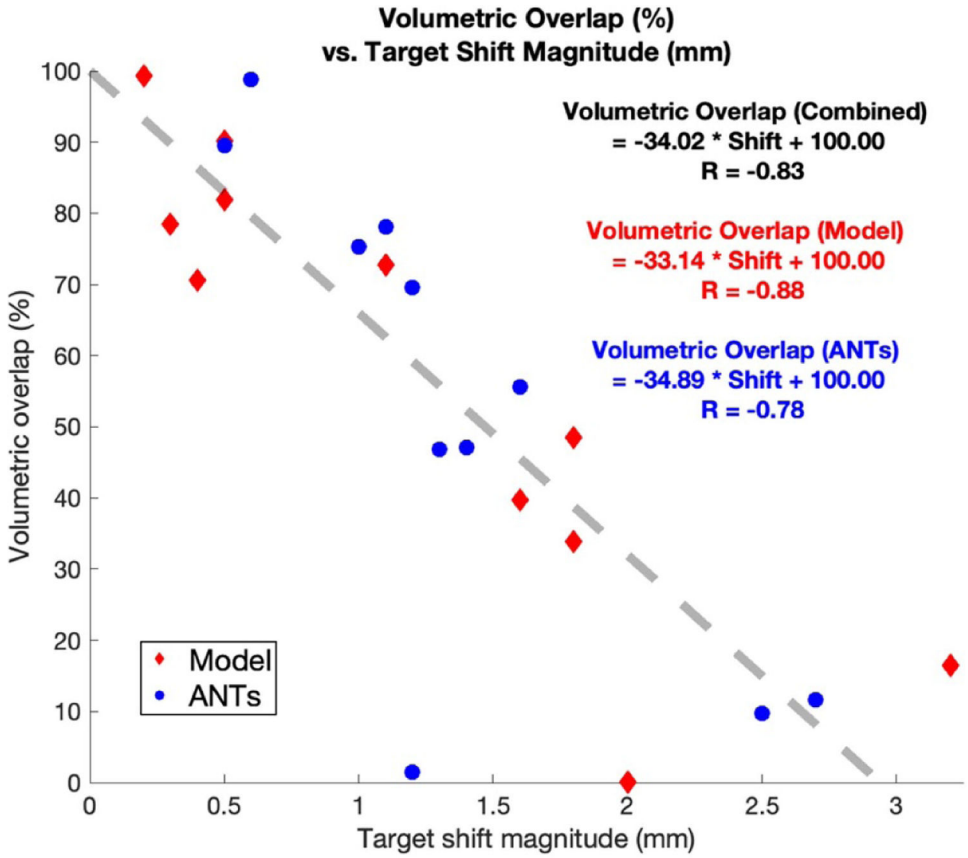

Figure 9.

Volumetric overlap vs. estimated shift at deep brain target region. Prediction via model-based approach in red; prediction via ANTs in blue. Linear regression is performed with Pearson CC for model (red), ANTs (blue) and combined data (black).

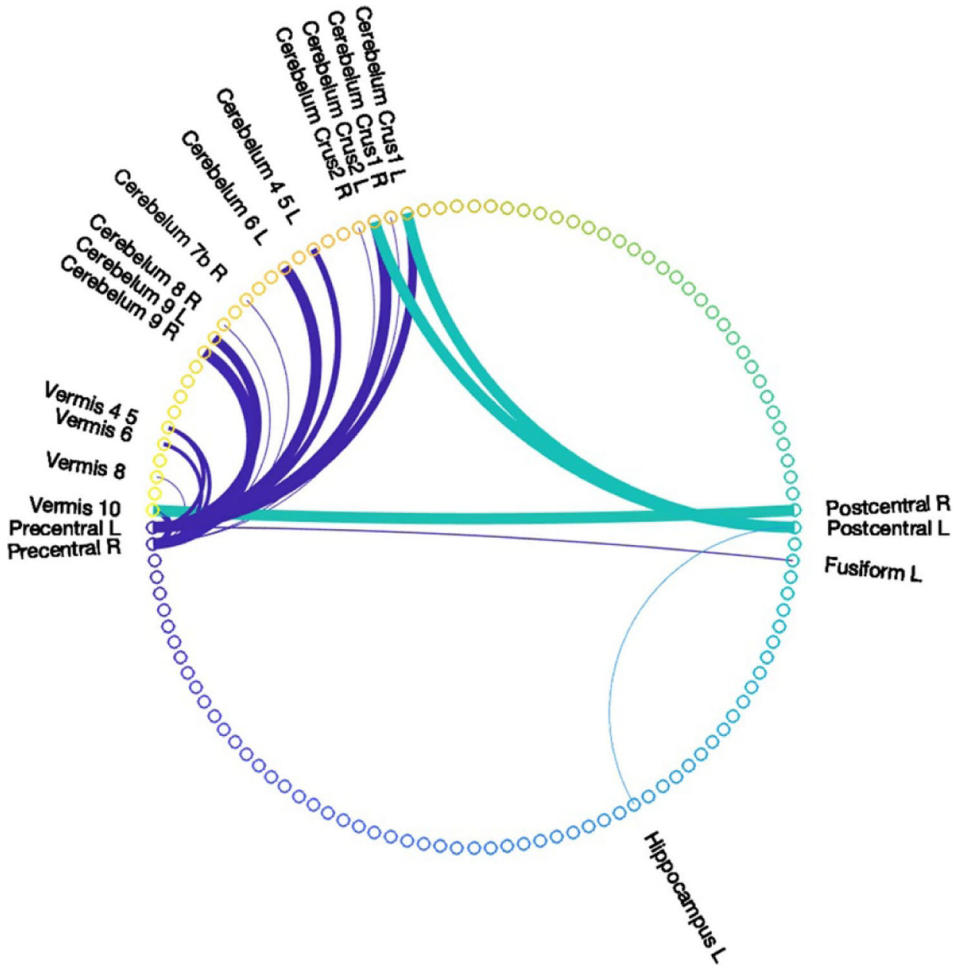

Figure 10.

Connectivity change of shift-considered connectivity matrices from without shift consideration with respect to precentral and postcentral gyri, where line width represents the extent of change.

Table 1.

Estimated shift at deep brain target region.

Case #	Right implant (mm)		Left implant (mm)	
	Model	**ANTs**	**Model**	**ANTs**
1	3.2	2.5	[a]	[a]
2	0.4	0.5	2.0	1.2
3	1.1	1.1	0.3	1.4
4	0.2	0.6	1.6	2.7
5	1.8	1.3	0.5	1.0
6	0.5	1.2	1.8	1.6
Average	1.2 ± 1.1	1.2 ± 0.7	1.2 ± 0.8	1.6 ± 0.7

[a]Indicates a unilateral implant.

Table 2.

Tract volume for right and left implants for each case with reconstructed electrode leads under different shift considerations.

	Tract volume (mm^3)		Tract volume percent change (%)	
	Without shift considered With model shift considered With ANTs shift considered		Model ANTs	
Case #	**Right implant**	**Left implant**	**Right implant**	**Left implant**
1	10 320	*a*	26.59	*a*
	14 058		22.20	
	13 265			
2	10194	616	22.42	92.85
	8327	8611	3.83	66.79
	9818	1855		
3	9253	10160	7.81	3.15
	10 037	9850	9.08	1.86
	10177	10 353		
4	10 624	9938	1.04	25.88
	10515	7895	1.35	51.89
	10 482	6543		
5	10 963	7385	49.32	3.42
	7342	7141	21.87	10.55
	8996	8256		
6	10 374	9857	5.50	40.57
	10 978	7012	22.89	6.57
	8442	9249		
Average	—	—	18.78	33.17
			27.53	13.54

[a] Indicates a unilateral implant.

Table 3.

Absolute change in volume overlap between predicted fiber bundles and motor regions of precentral and postcentral gyri.

	Overlapping volume difference (mm^3)	
	No shift vs. model-predicted shift No shift vs. ANTs-predicted shift	
Case #	**Right implant**	**Left implant**
1	208	*a*
	421	
2	235	151
	115	151
3	115	87
	206	374
4	0	372
	0	397
5	847	17
	246	278
6	190	212
	75	392

*a*Indicates a unilateral implant.

J Neural Eng. Author manuscript; available in PMC 2022 September 15.

Table 4.

Volumetric distribution of fiber bundles: overlap, and with shift considered (i.e. shifted-unique volume fraction) via model or ANTs and without shift consideration (i.e. unshifted-unique volume fraction). A Venn diagram is provided to further illustrate the three components of interest summarized in table 4 and their relations.

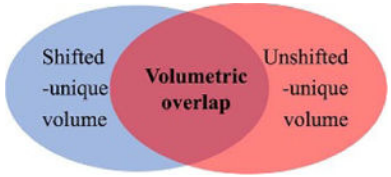

		With model-predicted shift profile			With ANTs-predicted shift profile		
Case #	**Implant description**	**Shifted-unique volume fraction (%)**	**Unshifted-unique volume fraction (%)**	**Volumetric overlap (%)**	**Shifted-unique volume fraction (%)**	**Unshifted-unique volume fraction (%)**	**Volumetric overlap (%)**
1	Right implant	33.04	50.49	16.48	38.00	52.28	9.72
	Left implant	*a*	*a*	*a*	*a*	*a*	*a*
2	Right implant	23.80	5.56	70.64	6.86	3.59	89.55
	Left implant	9.35	90.62	0.03	30.43	68.08	1.49
3	Right implant	9.67	17.53	72.80	5.95	15.94	78.11
	Left implant	13.07	8.52	78.41	26.74	26.14	47.12
4	Right implant	0.69	0.06	99.24	1.12	0.04	98.84
	Left implant	38.98	21.30	39.72	56.58	31.77	11.65
5	Right implant	40.92	10.63	48.45	31.66	21.53	46.81
	Left implant	6.46	3.41	90.13	8.37	16.30	75.32
6	Right implant	6.76	11.35	81.89	21.17	9.29	69.54
	Left implant	45.61	20.47	33.92	25.58	18.89	55.54

[a]Indicates a unilateral implant.